Fuel Processing Technology 221 (2021) 106935

Contents lists available at ScienceDirect

Fuel Processing Technology

journal homepage: www.elsevier.com/locate/fuproc

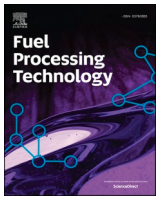

Effect of coal ash on the performance of $CuO@TiO_2$-Al_2O_3 in chemical looping with oxygen uncoupling

Jinchen Ma [a,1], Xin Tian [a,1], Haibo Zhao [a,*], Jingjing Ma [b], Chuguang Zheng [a]

[a] State Key Laboratory of Coal Combustion, Huazhong University of Science and Technology, Wuhan 430074, PR China
[b] Key Laboratory of High-efficiency Utilization of Coal and Green Chemical Engineering, Ningxia University, Yinchuan 750021, PR China

ARTICLE INFO

Keywords:
Chemical looping with oxygen uncoupling
Oxygen carrier
Coal
Ash

ABSTRACT

For the chemical looping with oxygen uncoupling (CLOU) process that fueled with coal, the release of the gaseous O_2 or the mobility of the lattice oxygen can be suppressed by coal ash deposition on the surface of the oxygen carrier (OC) or weakened by the interaction between the active phase of the OC and coal ash. In this work, we aim to identify the potential effects of coal ash on the performance of $CuO@TiO_2$-Al_2O_3 OC in CLOU. Over 50 redox cycles, the CO_2 yield was attained in the range of 92.1%–99.6%, indicating the stable redox reactivity of the $CuO@TiO_2$-Al_2O_3 OC. According to the XRD results, Ca was found to be deposited on the surface of the OC in the form of $Ca_2Al_2SiO_7$. However, a close-grained ash shell was avoided to cover the surface of OC due to the continuously gaseous O_2 by CuO. In addition, stable active phases (CuO and $CuAl_2O_4$) were detected in both of the fresh and used samples. Moreover, the consumption of CuO was avoided by the formation of $CaSO_4$ and $Ca_2Al_2SiO_7$. At last, the uniform distribution of Fe_2O_3 was detected and accumulated on the OC, which also act as the active phase of the OC.

1. Introduction

Chemical looping with oxygen uncoupling (CLOU) shows the merit of the inherent CO_2 separation in fossil fuel combustion, as realized by utilizing the gaseous O_2 released from transition metal oxides (also known as oxygen carrier, OC) instead of air [1]. Among all the potential oxygen carriers used in CLOU, CuO-based OC has been demonstrated as the one of the most promising candidates [2]. So far, Cu-based OCs [2–5] have been extensively investigated under the context of CLOU in terms of pollutant behaviors (sulfur [6], nitrogen [7,8], chlorine [9], and mercury [10]).

In CLOU of solid fuels, e.g., coal, the possible interaction between the active phase of Cu-based OC (CuO) and the mineral matters in coal ash (like Fe_2O_3 and CaO) can firstly generate Ca_2CuO_3 in the oxidation stage and then Cu_5FeS_4 in the reduction stage, respectively. Such kind of interactions would eventually lead to the decreased oxygen donation capacity of the OC [11]. Moreover, the interaction between Cu-based OC and typical elements of coal ash in CLOU was investigated by Saha et al. [12], Gong et al. [13] and Dai et al. [14] in thermal gravimetric analyzer (TGA), by mixing coal or high fractions of coal ash (33.3 wt% and 50 wt %) with the OC, respectively. Coal ash deposition on the OC was verified by the observation of Ca, Fe, Si and Al elements on the surface of the used OC samples. Gong et al. [13] revealed the physical and chemical effects of coal ash on the OC. With respect to the physical effect, the specific surface area and pore size of the OC both decreased, and the particles were sintered and agglomerated. In terms of the chemical effect, interaction between CuO and Al_2O_3 occurred and thus the activation energy for the gas-solid reaction increased. More importantly, the OC was seriously deactivated due to particle sintering during long-term redox cycles. Dai et al. [14] indicated that the sintering and agglomeration of the particles was probably attributed to the interaction between alkali species (Na and K) and OC. In addition, the sintering and agglomeration of the Cu-based particles could be quite different in the fluidized bed reactor and the fixed bed reactor in TGA, where the fluidization regime was different. In order to retain the donating capacity of CuO/Al_2O_3 OC, the interaction between CuO and Al_2O_3 was effectively suppressed by the introduction of micro-Al_2O_3 particles [15–17]. Within 12 redox cycles, the mole fraction of Al in $CuAl_2O_4$ increased by 3.36% for the used OC [10], which deserved to be evaluated for much longer redox reaction testing.

This work aimed to evaluate the performance of the core-shell $CuO@TiO_2$-Al_2O_3 oxygen carrier in 50 redox cycles. The deposition

* Corresponding author.
E-mail address: hzhao@mail.hust.edu.cn (H. Zhao).
[1] These authors contributed equally to this work.

https://doi.org/10.1016/j.fuproc.2021.106935
Received 25 February 2021; Received in revised form 21 May 2021; Accepted 6 June 2021
Available online 25 June 2021

Table 1
Ultimate and proximate analyses of PDS anthracite[a].

	Moisture	Volatile	Ash	Fixed carbon	C	H	N	S	O[b]
PDS (wt%)	1.88	14.98	16.87	66.27	64.73	3.99	1.08	0.30	11.15

[a] Air dried basis; [b]by difference.

Table 2
Main compositions of the PDS coal ash (wt%).

	SiO_2	Al_2O_3	CaO	SO_3	Fe_2O_3	K_2O	MgO	Na_2O	TiO_2	Others
PDS ash	52.66	28.10	6.53	3.90	3.31	1.70	1.51	1.02	0.86	0.41

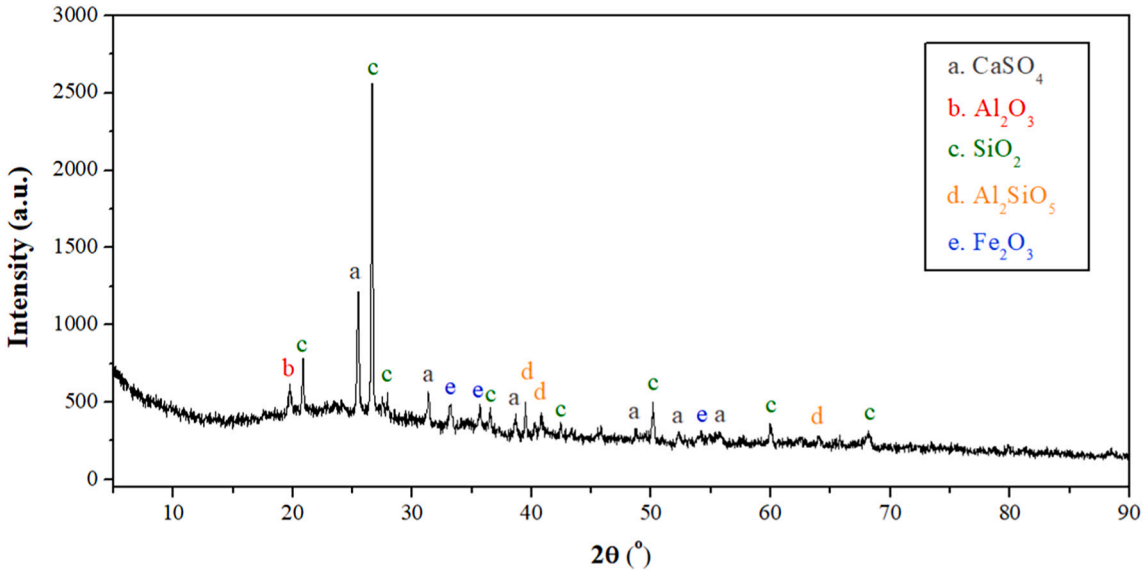

Fig. 1. XRD patterns of the PDS coal ash.

and interaction of coal ash on the OC was investigated by using the Pingdingshan (PDS) anthracite as the solid fuel, which has high fractions of Si and Al in ash (52.66 wt% SiO_2 and 28.10 wt% Al_2O_3). The microstructure and the distribution of typical elements in coal ash (Ca and Fe) on the surface of the used OC were identified by scanning electron microscopy (SEM) equipped with energy dispersive spectroscopy (EDS). X-ray fluorescence spectrometry (XRF) and X-Ray diffraction (XRD) were employed to determine the elements composition and crystal structure and morphology of both the fresh and used OC samples. At last, the surface composition of the used OC was determined by X-ray photoelectron spectroscopy (XPS). The behaviors or effects of the five main elements in PDS anthracite ash on the OC were discussed.

2. Material and methods

2.1. Materials

CuO@TiO_2-Al_2O_3 was used as the oxygen carrier (OC) in CLOU of PDS anthracite. The core-shell CuO@TiO_2-Al_2O_3 OC were prepared by the self-assembly template combustion synthesis (SATCS) method [15]. Firstly, μm-Al_2O_3 was used as the core, which was covered by the nano-TiO_2 (shell). Secondly, the slurry with the core shell template was stabilized by the addition of $CO(NH_2)_2$. Thirdly, a wet gel of $\{Cu[CO(NH_2)_2]_2\}^{2+}$ with urea molecules was synthetized by the addition of the

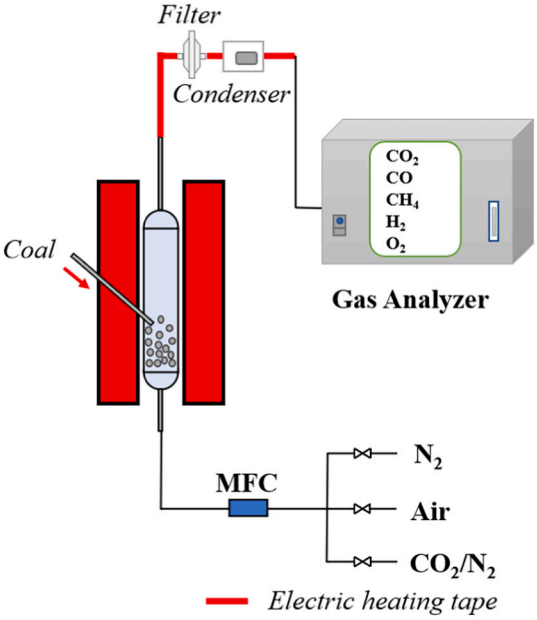

Fig. 2. Sketch map of the batch fluidized bed reactor.

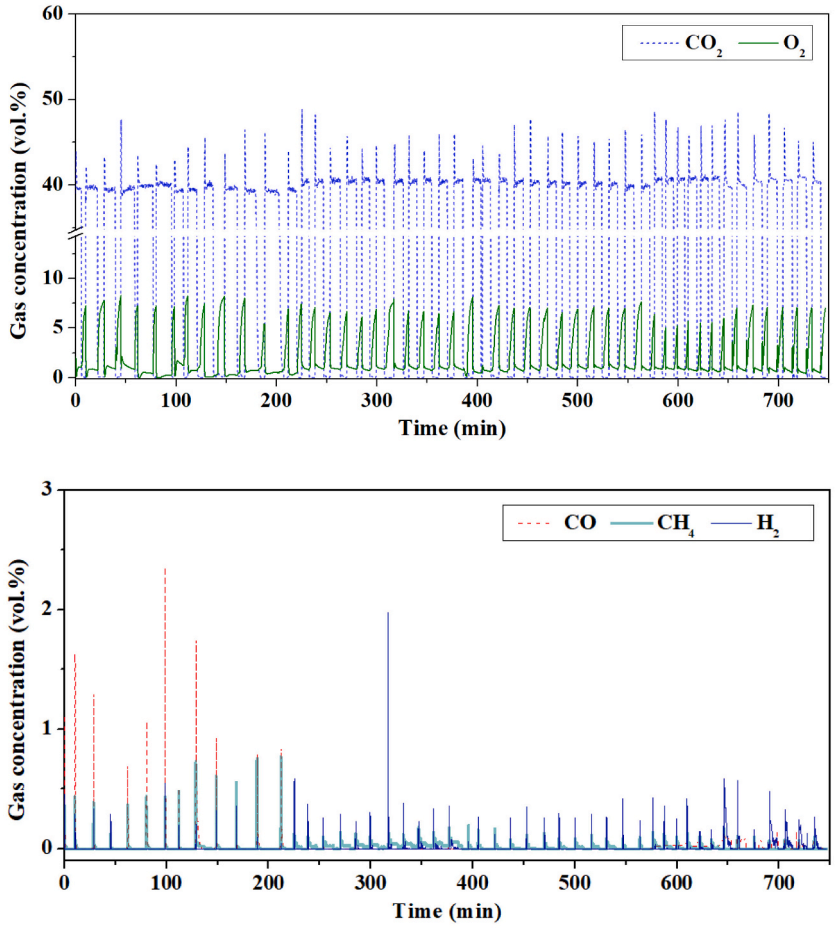

Fig. 3. Concentrations of gases (a. CO_2 and O_2; b. CO, CH_4, C_nH_m and H_2) during the 50 redox cycles.

copper nitrate ($Cu(NO_3)_2{\cdot}3H_2O$) into the slurry. Fourthly, drying and calcination processes were completed at 80 °C for 24 h and 950 °C for 2 h, respectively. Finally, CuO@TiO_2-Al_2O_3 OC particles (0.15–0.35 mm) were achieved with the main composition of 78.02 ± 0.21 wt% CuO, 5.95 ± 0.12 wt% TiO_2 and 13.60 ± 0.17 wt% Al_2O_3. Due to the nano-TiO_2 coverage on the external of micro-Al_2O_3, the reactivity of the OC could maintain well by suppressing the $CuAl_2O_4$ formation.

The PDS coal used was in the size range of 0.3–0.5 mm, and the ultimate and proximate analysis was shown in Table 1. The PDS coal ash was produced under the CO_2 gasification process and the oxidation process at 900 °C in the batch fluidized bed reactor. The coal ash compositions were determined by XRF and XRD, as shown in Table 2 and Fig. 1.

2.2. Experimental Setup

The geometric dimension of the batch fluidized bed reactor was 20 mm in diameter and 100 mm in height. Two sintered plates (an aperture diameter of 0.07 mm) were used as the distributor (the lower one in the reactor) and the protector (the upper one in the reactor), respectively, as shown in Fig. 2.

The fluidization gas was 2.0 L/min (5.6 U_{mf}, the minimal fluidization gas velocity). A complete redox cycle was composed by the reduction process (40 vol% CO_2 in N_2), purification process (100 vol% N_2), and the oxidation process (8.5 vol% O_2 in N_2). It should be noted that the ash fusion temperature of coal under char-CO_2 reaction condition is about 50–100 °C lower than that under char-H_2O reaction condition [18]. Therefore, the CO_2 was used as the gasification agent for the anthracite, where the OC could suffer in a worse CLOU environment. With this in mind, CO_2 was used as the gasification agent for the anthracite. The bed inventory of OC was 15 g OC and 0.213 g coal was injected into the reactor at the initial reduction process with an oxygen to fuel ratio of 2.80 [6].

2.3. Data evaluation

The total flow rate of the flue gas at the outlet of the reactor ($F_{out,\,j}$) is calculated based on N_2 balance, as $F_{out,\,j} = F_{N_2}/(1 - \sum c_i)$. F_{N_2} is the flow rate of N_2 into the reactor; c_i is the volume fraction of gas i (CO_2, CO, CH_4, H_2, and O_2) in flue gas; $F_{out,\,j}$ is the flow rate of the flue gas during the reduction process ($F_{out,\,re}$) or the oxidation process of OC ($F_{out,\,ox}$).

The carbon conversion during the reduction process, X_C, is calculated on the basis of the carbon balance within the whole reaction [19].

$$X_C = \left(\int_{t_0}^{t_{re}} F_{out,re}(c_{CO_2} + c_{CH_4} + c_{CO})dt - F_{CO_2,in} \right) \Big/ (22.4 m_C/12) \quad (1)$$

where $F_{CO_2,\,in}$ is the flow rate of CO_2 used as the gasification agent (0.8 L/min), m_C is the mass of carbon in coal.

The residual carbon ratio, $X_{C,\,OX}$, is calculated as,

$$X_{C,OX} = \left(\int_{t_0}^{t_{ox}} F_{out,ox}(c_{CO_2} + c_{CH_4} + c_{CO})dt \right) \Big/ (22.4 m_C/12) \quad (2)$$

The carbon balance is the sum of the X_C and $X_{C,\,OX}$.

Carbon capture efficiency, η_{CC}, is defined as the ratio of the carbon conversion during the reduction process to the total carbon conversion within the whole redox cycle.

$$\eta_{CC} = X_C/(X_C + X_{C,OX}) \quad (3)$$

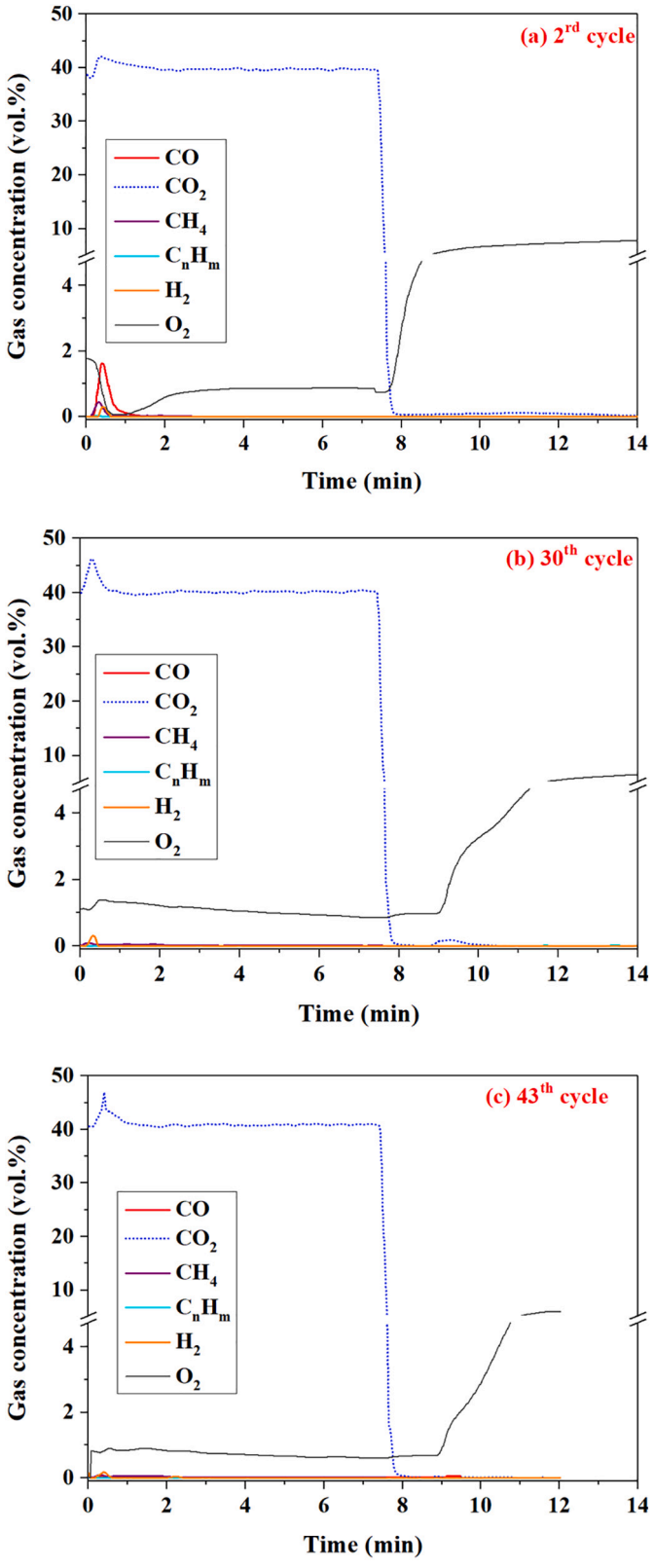

Fig. 4. Concentrations of the main carbonaceous gases and H_2 at the (a) 2rd redox cycle, (b) 30th redox cycle, and (c) 43th redox cycle.

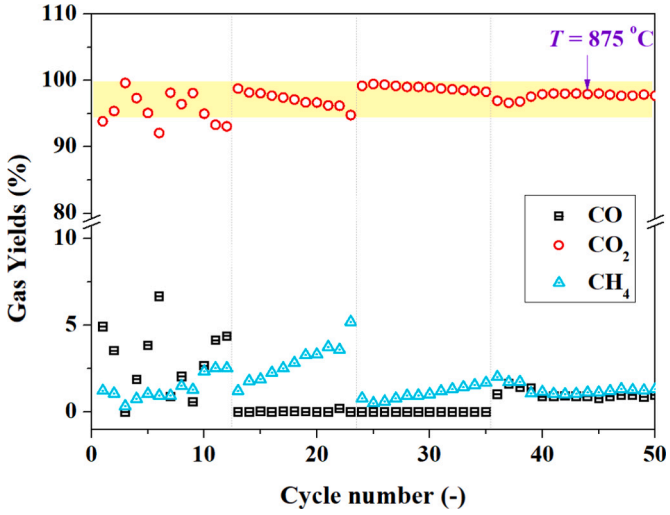

Fig. 5. Yields of CO_2, CO, and CH_4.

The gas yield (Y_i, i = CO_2, CO, and CH_4) is calculated based on the equations in the previous work [16].

$$Y_i = \frac{\int_0^{t_{fre}} F_{out,re} c_i dt}{\int_{t_0}^{t_{fre}} F_{out,re}(c_{CO_2} + c_{CH_4} + c_{CO})dt - F_{CO_2,in}} \quad (4)$$

The average apparent rate for carbon conversion to 0.95, $r_{X_C \le 0.95}$, was determined as,

$$r_{X_C \le 0.95} = 0.95/(t_{X_C=0.95} - t_0) \quad (5)$$

where $t_{X_C=0.95}$ represents the reaction time necessary to reach a char conversion of 95%.

3. Result and discussion

3.1. Gas concentrations in 50 cycles

The concentrations of the main carbonaceous gases and H_2 during the 50 redox cycles are shown in Fig. 3. Two operating temperatures were set, as 900 °C for the 1st–43th cycles and 875 °C for the 44th–50th cycles. The reduction time varied from 10 to 16 min in the 4th–6th and 10th–12th cycles and all the others' reduction time were 8 min. The coal was injected by a pulse of high-pressure N_2 (0.1 s and 0.3 Mpa) into the reactor when the concentration of CO_2 reached to 38.3 vol% - 40.2 vol% and the concentration of O_2 dropped to approximately 1.5 vol% (the O_2 equilibrium partial pressure for CuO at 900 °C [20]).

The CO_2 concentration was immediately increased to 42.2 vol %-48.5 vol% due to the oxidation of the volatiles and gasification products by the gaseous O_2 and the lattice oxygen provided by Cu-based OC. The average carbon balance was 1.04 ± 0.01, indicating the approximately complete carbon conversion (more details were shown in Section 3.3).

At the 1st-13th cycles, three kinds of the volatiles (CH_4, CO, and H_2) were detected during the reduction process. The reason for the unconverted gases (typical gases in the volatiles: CH_4 and CO) was due to the insufficient solid-gas contact. After the 14th cycle, the escaped gases were mainly CH_4 and H_2. The explanation was that CH_4 was derived from the volatiles and H_2 was from the methane reforming or the H_2O-gasification of the char because of the peak of H_2 behind that of CH_4,

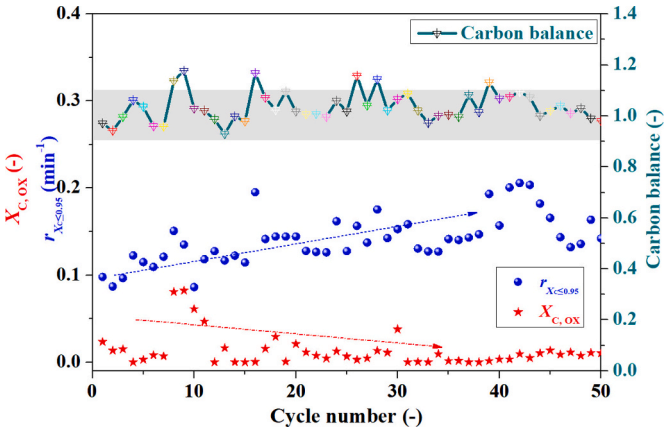

Fig. 6. Carbon balance, $r_{XC\leq0.95}$ and $X_{C,\ OX}$.

shown in Fig. 4 (b and c), compared to the reference test [10]. During the last 6 cycles at 875 °C, H_2 and CO concentrations became higher. It was attributed to the deactivation of OC and low reactivity of OC at 875 °C.

Concentrations of the main carbonaceous gases and H_2 during the representative cycles at the preliminary stage (2rd cycle), middle stage (30th cycle), and later stage (43th cycle) were shown in Fig. 4 (a-c). During the reduction process, CO_2 peaks were 3.89 vol%, 5.00 vol% and 6.39 vol% at the 2rd, 30th and 43th cycles, respectively. The CO and CH_4 peaks showed a decreasing trend in parallel. The OC could be activated after redox cycles [21,22]. In addition, the stable reactivity of this OC was attributed to the inhibition of $CuAl_2O_4$ formation by nano-TiO_2, as shown in Figs. 7 and 10. Moreover, a stable releasing gaseous O_2 (0.64 vol%-0.87 vol%) was observed during the later stage of the reduction process. Within the oxidation process, only a small amount of CO_2 was detected, resulting from the combustion of the residue char at the 2rd, 30th and 43th cycles.

3.2. Yields of CO_2, CO, and CH_4

The yields of CO_2, CO and CH_4 were shown in Fig. 5. The highest CO_2 yield of 99.6% was achieved at the 3rd cycle, while, the lowest CO_2 yield was 92.1% at the 6th cycle, during the 1st-12th cycles. The unconverted CH_4 indicated an incomplete conversion of the volatiles. It was because of the insufficient solid-gas contact caused by a slight agglomeration of the OC particles, as shown in the Fig. S1 in the supporting information. This phenomenon was also observed at the 36th–37th cycle with the CO_2 yields of 96.9% and 96.8%. In order to ameliorate the fluidization condition of the OC, the fluidization gas velocity was elevated to 3 L/min (8.4 U_{mf}). By this way, the CO_2 yield started to increase at the 38th cycle and became steady at 98.0% at 40th–43th cycles. At last, the operating temperature was decreased to 875 °C to alleviate the possible agglomeration or sintering of the OC particles within the 44th to 50th cycles. A stable CO_2 yields of 97.7% to 98.0% were attained. Satisfactory performance of CuO@TiO_2-Al_2O_3 was well maintained by adding the nano powders of TiO_2 to inhibit the formation of $CuAl_2O_4$.

3.3. Carbon balance, $r_{X_C\leq0.95}$, and $X_{C,\ OX}$

The carbon balance of 50 cycles ranged from 0.9 to 1.1 for 44 cycles and 1.1 to 1.2 for 6 cycles in Fig. 6, which was in a confidence interval. This result also indicated that the injected coal was completely converted in each cycle.

The average apparent rate for the carbon conversion to 0.95, $r_{XC\leq0.95}$, which can reflect the promotion of the OC on the char conversion rate, was further calculated. During the 43 cycles at 900 °C, the $r_{XC\leq0.95}$ showed an increasing trend from 0.1 min^{-1} to 0.2 min^{-1}, demonstrating a drop of the reaction time required to reach a char conversion of 95%. This result showed that the capacity to release gaseous O_2 and the reactivity of OC were maintained well, which was beneficial to enhancing the conversion or gasification of high-rank coal (PDS anthracite). Moreover, the presence of CaO could partly improve the carbon conversion [23,24]. The $r_{XC\leq0.95}$ of CuO@TiO_2-Al_2O_3 was double of that for the Cu-decorated hematite [25] and the agglomeration of CuO@TiO_2-Al_2O_3 was mild even though it contained a high content of Cu. This result confirmed that the nano-TiO_2 was favorable to maintain the structure of the OC by inhibiting the formation of $CuAl_2O_4$.

The residual carbon ratio, $X_{C,\ OX}$, was below 0.1 in average during 50 cycles. This result indicated that the char combustion or gasification was enhanced by gaseous O_2, lattice oxygen or the alkalis in the ash. The effect of the accumulated ash on the $X_{C,\ OX}$ was little.

Table 3
Main composition of the OC samples by XRF.

Oxygen carrier	CuO (wt %)	TiO_2 (wt%)	Al_2O_3 (wt%)	SiO_2 (wt%)	Fe_2O_3 (wt%)	CaO (wt %)
Fresh sample	78.02 ± 0.21	5.95 ± 0.12	13.60 ± 0.17	2.43 ± 0.08	–	–
Used sample (50 cycles)	72.80 ± 0.25	4.71 ± 0.11	16.43 ± 0.23	2.20 ± 0.16	1.35 ± 0.06	0.751 ± 0.037

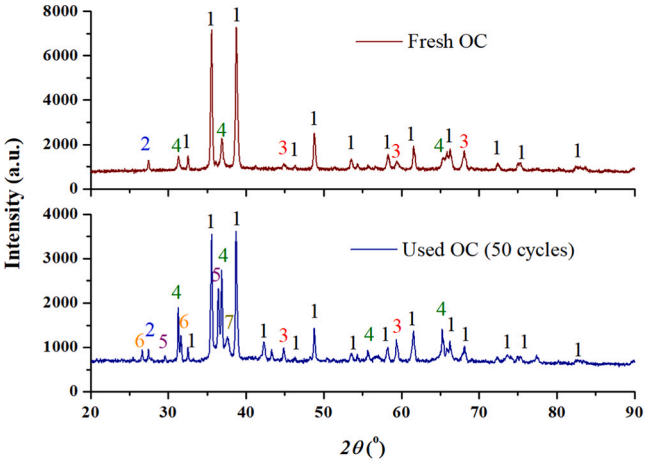

Fig. 7. XRD patterns of the fresh OC and the used OC (50 cycles).

4. Characterization of OC

4.1. Main compositions by XRF and XRD

The main compositions of the fresh and used samples were determined by XRF, as shown in Table 3. The mass fraction of the active phase (CuO) was reduced by 5.22 wt%. On the contrary, the mass fraction of Al_2O_3 was increased by 2.83 wt%. The new phases, i.e., Fe_2O_3 and CaO, were detected in the used samples (mixed OC and ash). Nevertheless, the deposited Fe_2O_3 and CaO on the OC cannot be distinguished and thus was further identified by SEM + EDS in the following section.

The fresh sample was composed by the CuO, TiO_2, Al_2O_3 and $CuAl_2O_4$ in Fig. 7. For the used sample, the peak of $CuAl_2O_4$ increased, which semi-quantitatively indicated that more $CuAl_2O_4$ formed during 50 redox cycles. The main phases of the ash, e.g. $CaSO_4$, $Ca_2Al_2SiO_7$, and SiO_2, were detected both in the simple coal ash sample and the mixed sample of coal ash and the used OC samples. The sulfur in coal was fixed by CaO in the coal ash, thus the formation of $CuSO_4$ can avoid. This result was similar to the sulfur behavior in the CLC of the Xiaolongtan lignite [6]. Hence, the CaO in the ash protected the Cu-based OC by the

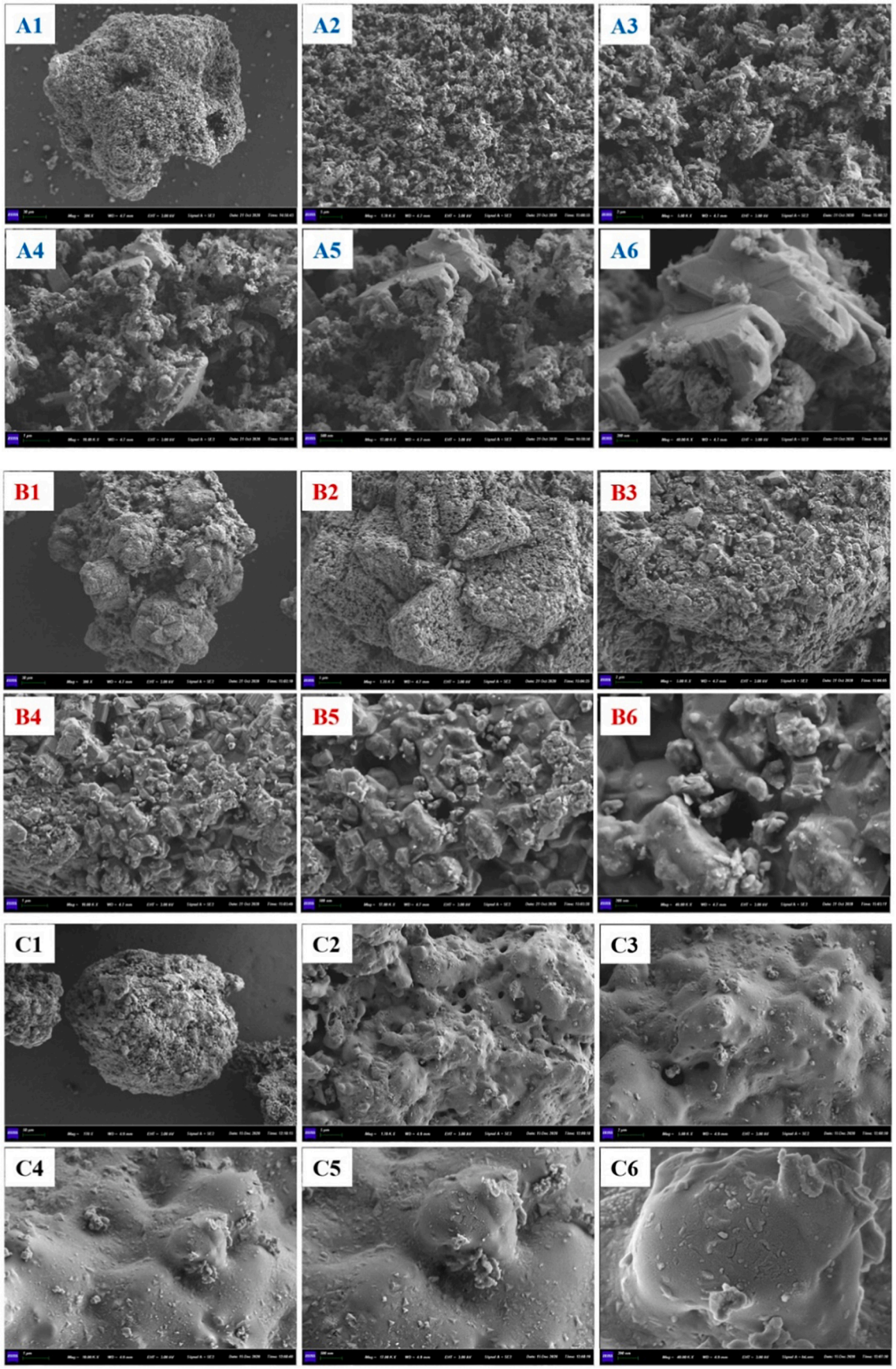

Fig. 8. SEM images of the (A) fresh OC and the used OCs (B) 23 cycle, and (C) 50 cycles.

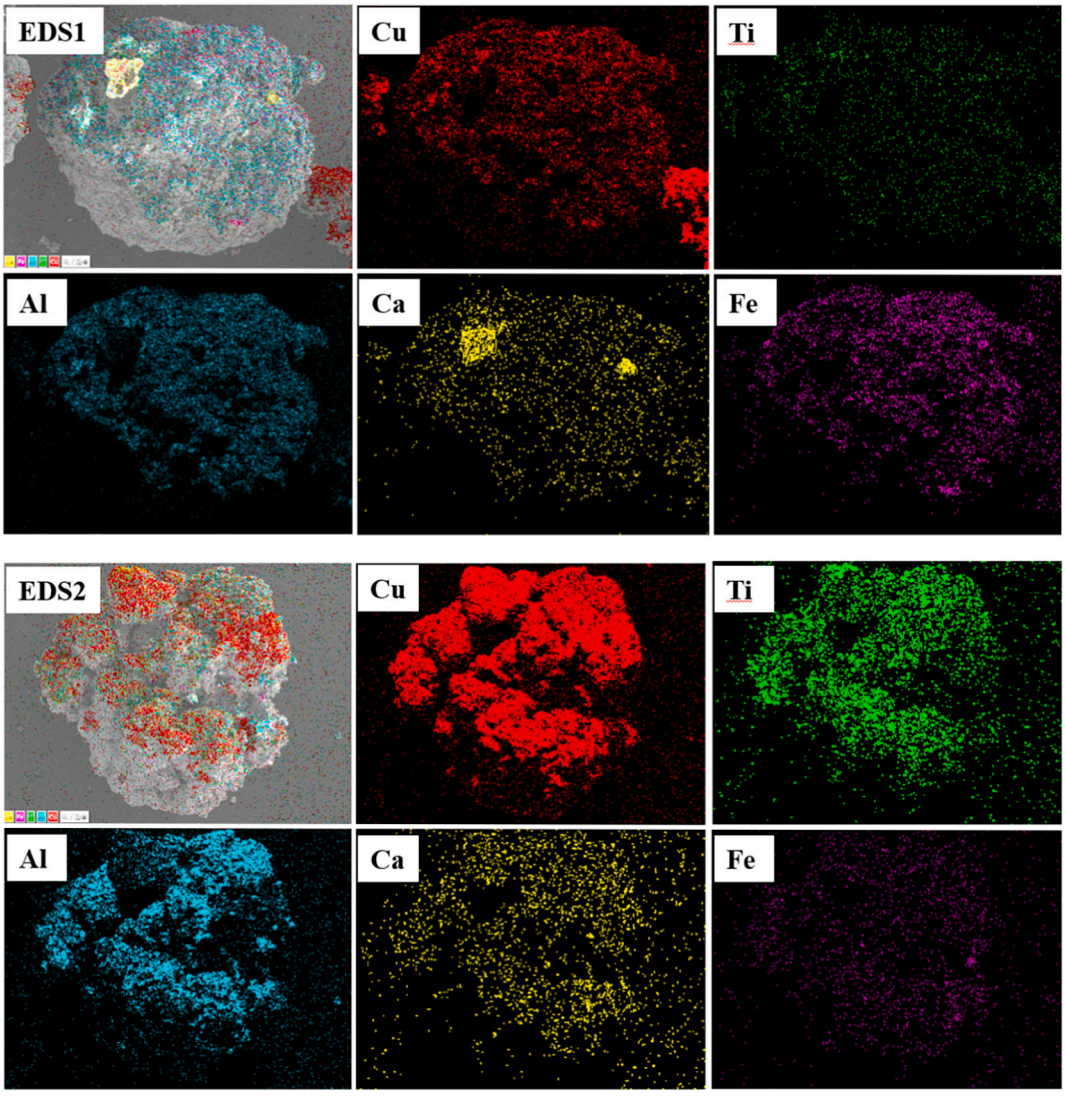

Fig. 9. EDS image of two used OC sample particles (after 50 cycles).

suppressed generation of the $CuSO_4$ or $Cu_2Al_2SiO_7$.

4.2. Microstructure

The good sphericity of the fresh OC (Fig. 8 (A1-A6)) and used OC (Fig. 8 (B1-B6) and (C1-C6)) were verified by the SEM.

A melt polycondensation and densification was observed on the used OC (after 23 cycles) in Fig. 8 (B1-B2). Specially, the cementation between the micro particles and small holes were observed in Fig. 8 (B5-B6), which was caused by the external diffusion of gaseous O_2 [26].

Moreover, an OC particle was covered by the ash, as shown in Fig. 8 (C1-C2). A plenty of the micropores (2–5 μm) were generated on the surface of the OC even though a part of the OC surface was covered by coal ash.

It should be noted that the more ash was accumulated and thus the contact of the coal ash and OC was sufficient. From this respect, more OC particles were covered by the coal ash, as shown in Fig. 9 (EDS1). While, some OC particles were little affected by the ash as shown in Fig. 9 (EDS2).

In the EDS1, the Ca deposition was concentrated on the surface of the OC particle, while the Fe was uniformly distributed. Nevertheless, the Ca and Fe could both promote the reactivity of the OC to some extent [23, 24].

The mass fractions of Fe and Ca were 19.80 wt% and 4.39 wt% (Fig. 9 EDS1), respectively, which was explained by that the mechanical strength of Fe_2O_3 was larger than those of $Ca_2Al_2SiO_7$, $CaSO_4$, and CaO. In addition, the fractions of Cu, Ti, and Al on the OC (after 50 cycles) were 34.16 wt%, 3.94 wt%, and 37.71 wt%, respectively, shown in EDS1. Moreover, Cu, Ca and Fe were all uniformly distributed on some OC particles. The fractions of Cu, Ti, Al, Fe, and Ca on the surface of the OC (after 50 cycles) were 71.38 wt%, 7.37 wt%, 18.80 wt%, 1.76 wt%, and 0.69 wt%, respectively. The fraction of the Cu decreased by 7.24 wt % in the used sample in comparison with the fresh sample [10]. The more fraction of the Al was resulted from the inner Al_2O_3 particle in the original OC and the Al_2O_3 in the deposited ash.

4.3. Surface composition by XPS

The surface composition of the used OC was determined by XPS. CuO was the main phase at the peaks of 932.7 eV and 933.8 eV in Fig. 10 (a). $CuSO_4$ (peak at 935.5 eV) was generated after 50 cycles and the mole fraction of the $CuSO_4$ was 9.38% on the surface of the used OC. The mole fraction of the $CuSO_4$ was increased by 0.66% during 37 cycles when compared with the previous work [10]. This result indicated that the CaO in the ash was conducive to consume the sulfate radical and so as to avoid the formation of $CuSO_4$ [27].

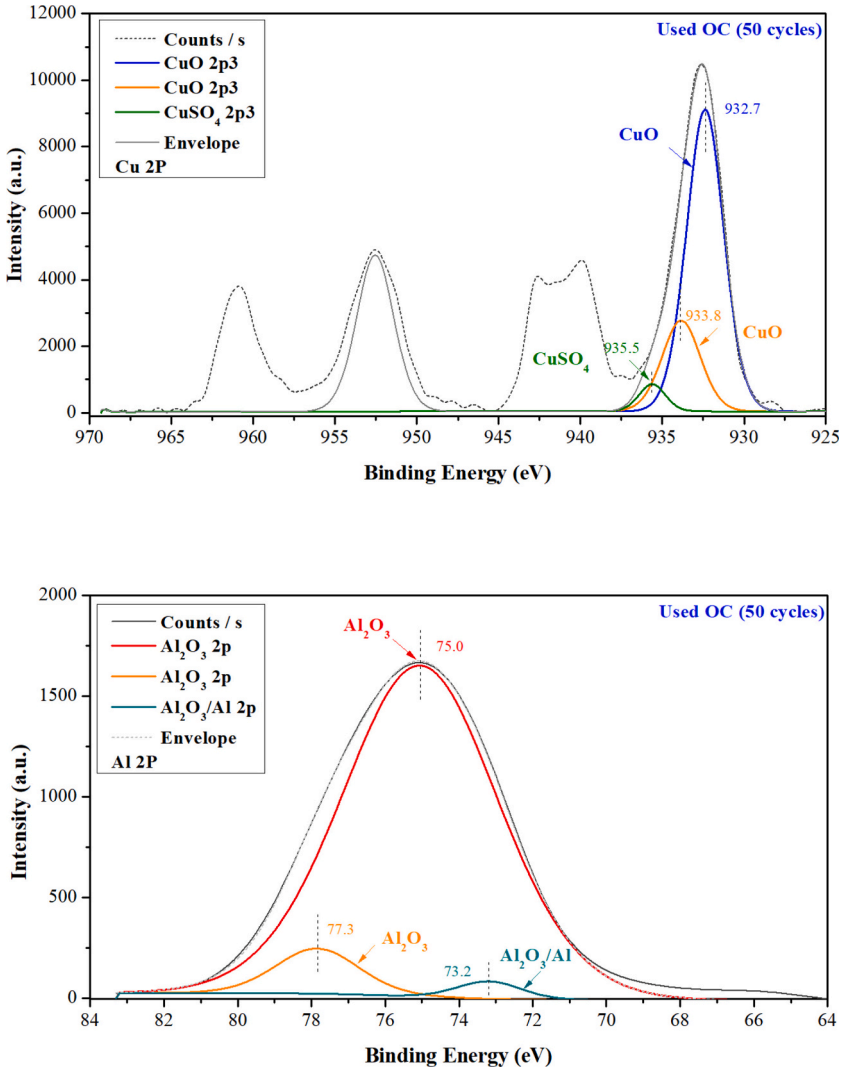

Fig. 10. XPS spectra of Cu and Al for the used OC (50 cycles).

Al_2O_3 (peaks at 73.2 eV, 75.0 eV, and 77.3 eV) was detected as a sole substance containing aluminum in Fig. 10 (b). No $CuAl_2O_4$ was detected on the surface of the OC. This result demonstrated a little formation of $CuAl_2O_4$, which can't be determined by XPS. However, the mole fraction of the $CuAl_2O_4$ was 4.17% after 13 cycles in the previous work [10]. Combined with the XRF analysis, the mole fraction of Cu in the $CuAl_2O_4$ was 0.65%. All these results indicated an effectively inhibiting effect of TiO_2 on the reaction between CuO and Al_2O_3.

5. Discussion

The main elements in the PDS anthracite (Si, Al, Ca, S, and Fe) showed different effects on the performance of the CuO@TiO_2-Al_2O_3.

Si: The formation of SiO_2 and Al_2SiO_5 was detected in the ash produced by the gasification and oxidation processes. The stable SiO_2 also remained in the mixed OC and ash in Fig. 7. The gehlenite ($Ca_2Al_2SiO_7$) was formed by the Al_2SiO_5 and CaO, which was highly correlative to the SiO_2/Al_2O_3 ratio (S/A) [28]. In addition, it was also a stable crystal phases above 1200 °C [28]. However, the formation of the $Ca_2Al_2SiO_7$ could cause the agglomeration of the OC particles.

Al: Al existed in the form of Al_2O_3 and Al_2SiO_5 in the ash. Al_2O_3 was detected as the main form on the surface of the used OC in Fig. 10 (b). A part of the element Al participated in the formation of $Ca_2Al_2SiO_7$ via $2CaO + Al_2O_3 + SiO_2 = Ca_2Al_2SiO_7$. Another part of the element Al could react with CuO to generate $CuAl_2O_4$ via $CuO + Al_2O_3 = CuAl_2O_4$ [13, 14], as indicated by the XRD in Fig. 7.

Ca: The favorable factors the performance of the OC were: the functions of the sulfur fixation [6], the promotion on the char gasification [29], and the consumption of Al_2SiO_5. Whereas, the formation of the $Ca_2Al_2SiO_7$ could partly covered the surface of the OC [30], which resulted in a decrease of contact between OC and combustible gases. It was advantageous that the pores were observed in the cover ($Ca_2Al_2SiO_7$) on the used OC sample in Fig. 8 (C2-C3). Thus, the capacity to release O_2 was just partially affected during the long-term redox cycles. Moreover, the $Ca_2Al_2SiO_7$ could be rubbed off in the fluidized bed reactor, which was indicated the CaO/Fe_2O_3 ratio in the used OC was lower to that in the ash in Table 2 and Fig. 9.

S: Part of the sulfur was fixed by CaO in the ash and some was formed as $CuSO_4$ in Fig. 10 (a). The equilibrium constant of the reaction ($CuO + H_2SO_4 = CuSO_4 + H_2O$) was lower than that of reaction ($CaO + H_2SO_4 = CaSO_4 + H_2O$), as shown in Fig. S2 in SM. Thus, the more redox cycles or the continuous test should be conducted in future work and the CaO-decorated CuO could restrain the formation of the copper sulfate [27].

Fe: The element Fe was uniformly distributed on the surface of the OC in Fig. 9. The mass fraction of the Fe on the surface was as high as 19.80 wt% in some OC particles and low to 1.76 wt% in other used OC. No $CuFe_2O_4$ was detected by the XPS analysis in Fig. 10 (c). Moreover, Fe_2O_3 phase could provide more lattice oxygen [31].

At last, it should be noted that the most suitable reactor for CLOU was the interconnected fluidized bed reactor, where the solid-gas fluidization and the separation of OCs in the cyclone was quite different from this batch fluidized bed reactor. In the continuous reactor, the agglomeration or sintering of the OC particles could be relieved due to a better heat transfer in a large reactor. Secondly, the ash could be peeled off the OC particles by the attrition between OC particles or the OC and reactor. Thus, the mildly agglomerated OC particles could be separated in the high-flux riser and cycles, where the gas velocity was reached to 8–10 m/s and 15–25 m/s, respectively. In the cyclone, part of the coal ash could be collected by the different densities of the particles [32]. At last, the OC could be totally covered by the ash within the continuously operation [30].

In summary, the formation of $Ca_2Al_2SiO_7$ should be avoided to cover the surface of the OC or cause the agglomeration of the OC particles. The copper sulfate was inhibited by the CaO in the ash. The CaO and Fe_2O_3 showed positive effects on the OC.

6. Conclusions

The performance of CuO@TiO_2-Al_2O_3 in the CLOU of the PDS antericite was evaluated at a batch fluidized bed reactor. The fractions of the SiO_2 and Al_2O_3 in the ash was high with a value of 52.66 wt% and 28.10 wt%, respectively. The CO_2 yield maintained at a relative high level (97.3%) after 50 cycles. The residual carbon ratio was <0.1 even though the PDS anthrecite was difficult to gasification.

The edges and corners of the OC sample disappeared after 50 redox cycles and a combined and mellow of the skeleton was formed on the surface of some OC patciles. Many holes with a diamater of 1 to 5 μm were generated by the O_2 releasing capability of the CuO, which developed a porous structure and prevented the complete cover of the coal ash on the surface of the OC.

Some positive effects of the elements in the ash were observed. The sulfur fixation of the Ca made a contribution to the stable reactivity of OC by reducing the possibility of the reaction between CuO and SO_4^{2-}. Moreover, the reaction between CaO and $Al_2SiO_7^{4-}$ also minimized the loss of active phase of CuO in the OC. Secondly, the deposited Fe on the OC samples can act as the active phase. Thirdly, the element Si could form the $Ca_2Al_2SiO_7$ with a low melting point, which could cover the surface or deposit on the pores or channels of the OC particles. It will cause a decreased contact between the combustible gases ($CO/CH_4/H_2$) and OCs or the agglomeration of the OC particles.

Declaration of Competing Interest

The authors declare that they have no known competing financial interests or personal relationships that could have appeared to influence the work reported in this paper.

Acknowledgements

This work was supported by the National Key R&D Program of China (No. 2016YFB0600801), National Natural Science Foundation of China (No. 52025063 and 51906076) and Fundamental Research Funds for the Central Universities(No. 2021XXJS066). Thanks to the Foundation of State Key Laboratory of High-efficiency Utilization of Coal and Green Chemical Engineering (Grant No. 2021-K08 and 2021-K38). The staff from the Analytical and Testing Center at Huazhong University of Science and Technology are appreciated for the relevant analytical work.

Appendix A. Supplementary data

Supplementary data to this article can be found online at https://doi.org/10.1016/j.fuproc.2021.106935.

References

[1] M. Ishida, H. Jin, A new advanced power-generation system using chemical-looping combustion, Energy 19 (1994) 415–422, https://doi.org/10.1016/0360-5442(94)90120-1.
[2] H. Zhao, X. Tian, J. Ma, X. Chen, M. Su, C. Zheng, Y. Wang, Chemical looping combustion of coal in China: Comprehensive progress, remaining challenges, and potential opportunities, Energy Fuel 34 (2020) 6696–6734, https://doi.org/10.1021/acs.energyfuels.0c00989.
[3] Y. Wang, X. Tian, H. Zhao, K. Liu, The use of a low-cost oxygen carrier prepared from red mud and copper ore for in situ gasification chemical looping combustion of coal, Fuel Process. Technol. 205 (2020) 106460, https://doi.org/10.1016/j.fuproc.2020.106460.
[4] Y. Qiu, L. Ma, M. Li, D. Cui, S. Zhang, D. Zeng, R. Xiao, Copper and cobalt co-doped ferrites as effective agents for chemical looping CO_2 splitting, Chem. Eng. J. 387 (2020) 124150, https://doi.org/10.1016/j.cej.2020.124150.
[5] J. Ma, D. Mei, W. Peng, X. Tian, D. Ren, H. Zhao, On the high performance of a core-shell structured CaO-CuO/MgO@Al_2O_3 material in calcium looping integrated with chemical looping combustion (CaL-CLC), Chem. Eng. J. 368 (2019) 504–512, https://doi.org/10.1016/j.cej.2019.02.188.
[6] J. Ma, D. Mei, C. Wang, X. Tian, Z. Liu, H. Zhao, Sulfur fate during in-situ gasification chemical looping combustion (iG-CLC) of coal, Chem. Eng. J. 406 (2021) 126773, https://doi.org/10.1016/j.cej.2020.126773.
[7] H. Gu, L. Shen, Z. Zhong, N. Xin, H. Ge, Y. Zhou, X. Shen, S. Jiang, NO release during chemical looping combustion with iron ore as an oxygen carrier, Chem. Eng. J. 264 (2015) 211–220, https://doi.org/10.1016/j.cej.2014.11.083.
[8] J. Ma, X. Tian, Z. Liu, H. Zhao, Fate of fuel-nitrogen during in situ gasification chemical looping combustion of coal, Fuel Process. Technol. 215 (2021) 106710, https://doi.org/10.1016/j.fuproc.2020.106710.
[9] J. Dai, K.J. Whitty, Impact of fuel-derived chlorine on CuO-based oxygen carriers for chemical looping with oxygen uncoupling, Fuel 263 (2020) 116780, https://doi.org/10.1016/j.fuel.2019.116780.
[10] J. Ma, X. Tian, B. Zhao, X. Li, Y. Zhao, H. Zhao, C. Zheng, Behavior of mercury in chemical looping with oxygen uncoupling of coal, Fuel Process. Technol. 216 (2021) 106747, https://doi.org/10.1016/j.fuproc.2021.106747.
[11] M. Keller, M. Arjmand, H. Leion, T. Mattisson, Interaction of mineral matter of coal with oxygen carriers in chemical-looping combustion (CLC), Chem. Eng. Res. Des. 92 (2014) 1753–1770, https://doi.org/10.1016/j.cherd.2013.12.006.
[12] C. Saha, S. Zhang, R. Xiao, S. Bhattacharya, Chemical Looping Combustion (CLC) of two Victorian brown coals – part 2: Assessment of interaction between CuO and minerals inherent in coals during multi cycle experiments, Fuel 96 (2012) 335–347, https://doi.org/10.1016/j.fuel.2012.01.048.
[13] R. Gong, C. Qin, D. He, L. Tan, J. Ran, Oxygen uncoupling of Cu-based oxygen carrier with the presence of coal ash in chemical looping process, Energy Fuel 32 (2018) 7708–7717, https://doi.org/10.1021/acs.energyfuels.8b01090.
[14] J. Dai, K. Whitty, Effects of coal ash on cuo as an oxygen carrier for chemical looping with oxygen uncoupling, Energy Fuel 32 (2018) 11656–11665, https://doi.org/10.1021/acs.energyfuels.8b02521.
[15] Z. Xu, H. Zhao, Y. Wei, C. Zheng, Self-assembly template combustion synthesis of a core-shell CuO@TiO_2-Al_2O_3 hierarchical structure as an oxygen carrier for the chemical-looping processes, Combust. Flame 162 (2015) 3030–3045, https://doi.org/10.1016/j.combustflame.2015.05.006.
[16] X. Tian, Y. Wei, H. Zhao, Evaluation of a hierarchically-structured CuO@TiO_2-Al_2O_3 oxygen carrier for chemical looping with oxygen uncoupling, Fuel 209 (2017) 402–410, https://doi.org/10.1016/j.fuel.2017.08.022.
[17] H. Zhao, X. Tian, J. Ma, M. Su, B. Wang, D. Mei, Development of tailor-made oxygen carriers and reactors for chemical looping processes at Huazhong University of Science & Technology, Int. J. Greenh. Gas Con. 93 (2020), 102898, https://doi.org/10.1016/j.ijggc.2019.102898.
[18] X. Wu, Z. Zhang, G. Piao, X. He, Y. Chen, N. Kobayashi, S. Mori, Y. Itaya, Behavior of mineral matters in Chinese coal ash melting during char-CO_2/H_2O gasification reaction, Energy Fuel 23 (2009) 2420–2428, https://doi.org/10.1021/ef801002n.
[19] T. Mendiara, P. Gayán, A. Abad, L.F. de Diego, F. García-Labiano, J. Adánez, Performance of a bauxite waste as oxygen-carrier for chemical-looping combustion using coal as fuel, Fuel Process. Technol. 109 (2013) 57–69, https://doi.org/10.1016/j.fuproc.2012.09.038.
[20] M. Su, H. Zhao, X. Tian, The competition between direct gas-solid reduction and oxygen uncoupling of CuO oxygen carrier in chemical looping with oxygen uncoupling: a single particle simulation study, Combust. Flame 221 (2020) 219–227, https://doi.org/10.1016/j.combustflame.2020.07.043.
[21] A. Cuadrat, A. Abad, J. Adánez, L.F. de Diego, F. García-Labiano, P. Gayán, Behavior of ilmenite as oxygen carrier in chemical-looping combustion, Fuel Process. Technol. 94 (2012) 101–112, https://doi.org/10.1016/j.fuproc.2011.10.020.
[22] L.F. de Diego, A. Abad, A. Cabello, P. Gayán, F. García-Labiano, J. Adánez, Reduction and oxidation kinetics of a $CaMn_{0.9}Mg_{0.1}O_{3-\delta}$ oxygen carrier for chemical-looping combustion, Ind. Eng. Chem. Res. 53 (2014) 87–103, https://doi.org/10.1021/ie4015765.
[23] H. Gu, L. Shen, Z. Zhong, Y. Zhou, W. Liu, X. Niu, H. Ge, S. Jiang, L. Wang, Interaction between biomass ash and iron ore oxygen carrier during chemical looping combustion, Chem. Eng. J. 277 (2015) 70–78, https://doi.org/10.1016/j.cej.2015.04.105.
[24] G. Schwebel, H. Leion, W. Krumm, Comparison of natural ilmenites as oxygen carriers in chemical-looping combustion and influence of water gas shift reaction on gas composition, Chem. Eng. Res. Des. 90 (2012) 1351–1360, https://doi.org/10.1016/j.cherd.2011.11.017.

[25] W. Yang, H. Zhao, J. Ma, D. Mei, C. Zheng, Copper-decorated hematite as an oxygen carrier for in situ gasification chemical looping combustion of coal, Energy Fuel 28 (2014) 3970–3981, https://doi.org/10.1021/ef5001584.
[26] R.F. Pachler, K. Mayer, S. Penthor, M. Kollerits, H. Hofbauer, Fate of sulfur in chemical looping combustion of gaseous fuels using a copper-based oxygen carrier, Int. J. Greenh. Gas Con. 71 (2018) 86–94, https://doi.org/10.1016/j.ijggc.2018.02.006.
[27] X. Tian, K. Wang, H. Zhao, M. Su, Chemical looping with oxygen uncoupling of high-sulfur coal using copper ore as oxygen carrier, P. Combust. Inst. 36 (2016) 3381–3388, https://doi.org/10.1016/j.proci.2016.08.056.
[28] J. Li, X. Wang, B. Wang, J. Zhao, Y. Fang, Effect of silica and alumina on petroleum coke ash fusibility, Energy Fuel 31 (2017) 13494–13501, https://doi.org/10.1021/acs.energyfuels.7b02843.
[29] B. Bhui, V. Prabu, Chemical looping based co-combustion of high ash Indian coal and rice straw operating under CO_2 in-situ gasification mode, J. Energy Inst. 94 (2020) 176–190, https://doi.org/10.1016/j.joei.2020.07.004.
[30] A. Corcoran, J. Marinkovic, F. Lind, H. Thunman, P. Knutsson, M. Seemann, Ash properties of ilmenite used as bed material for combustion of biomass in a circulating fluidized bed boiler, Energy Fuel 28 (2014) 7672–7679, https://doi.org/10.1021/ef501810u.
[31] J. Bao, Z. Li, N. Cai, Interaction between iron-based oxygen carrier and four coal ashes during chemical looping combustion, Appl. Energy 115 (2014) 549–558, https://doi.org/10.1016/j.apenergy.2013.10.051.
[32] J. Ma, H. Zhao, X. Tian, Y. Wei, S. Rajendran, Y. Zhang, S. Bhattacharya, C. Zheng, Chemical looping combustion of coal in a 5kWth interconnected fluidized bed reactor using hematite as oxygen carrier, Appl. Energy 157 (2015) 304–313, https://doi.org/10.1016/j.apenergy.2015.03.124.